

# X-ray scattering study of the spin-Peierls transition and soft phonon behavior in TiOCl

E.T. Abel<sup>1</sup>, K. Matan<sup>1</sup>, F.C. Chou<sup>2</sup>, E.D. Isaacs<sup>3</sup>, D.E. Moncton<sup>1</sup>, H. Sinn<sup>4</sup>, A. Alatas<sup>4</sup>, and Y.S. Lee<sup>1\*</sup>

<sup>1</sup>*Department of Physics, Massachusetts Institute of Technology, Cambridge, MA 02139*

<sup>2</sup>*Center for Condensed Matter Sciences, National Taiwan University, Taipei 10617, Taiwan*

<sup>3</sup>*Center for Nanoscale Materials, Argonne National Laboratory, Argonne, IL 60439 and*

<sup>4</sup>*Advanced Photon Source, Argonne National Laboratory, Argonne, IL 60439*

(Dated: February 1, 2008)

We have studied the  $S = 1/2$  quasi-one-dimensional antiferromagnet TiOCl using single crystal x-ray diffraction and inelastic x-ray scattering techniques. The Ti ions form staggered spin chains which dimerize below  $T_{c1} = 66$  K and have an incommensurate lattice distortion between  $T_{c1}$  and  $T_{c2} = 92$  K. Based on our measurements of the intensities, wave vectors, and harmonics of the incommensurate superlattice peaks, we construct a model for the incommensurate modulation. The results are in good agreement with a soliton lattice model, though some quantitative discrepancies exist near  $T_{c2}$ . The behavior of the phonons has been studied using inelastic x-ray scattering with  $\sim 2$  meV energy resolution. For the first time, a zone boundary phonon which softens at the spin-Peierls temperature  $T_{SP}$  has been observed. Our results show reasonably good quantitative agreement with the Cross-Fisher theory for the phonon dynamics at wave vectors near the zone boundary and temperatures near  $T_{SP}$ . However, not all aspects of the data can be described, such as the strong overdamping of the soft mode above  $T_{SP}$ . Overall, our results show that TiOCl is a good realization of a spin-Peierls system, where the phonon softening allows us to identify the transition temperature as  $T_{SP} = T_{c2} = 92$  K.

## I. INTRODUCTION

Understanding the properties of low-dimensional spin-1/2 systems remains a central challenge in condensed matter physics. In quasi-one-dimensional materials, a variety of ground-states can be stabilized, depending on the subtle interactions beyond the dominant magnetic exchange along the spin chain. For example, the low-energy physics of the  $S = 1/2$  Heisenberg spin chain[1, 2] becomes modified once coupling to the three-dimensional crystal lattice is taken into account. In the presence of spin-phonon coupling, the ground-state is dimerized, corresponding to the spin-Peierls state.[3, 4] If inter-chain magnetic interactions are significant, they can promote Néel order as an alternate ground state. Even though many quasi-one-dimensional  $S = 1/2$  spin chain materials have been studied so far, only a relatively small fraction are observed to have spin-Peierls ground states. The effects of the spin-phonon coupling in these and other low dimensional quantum spin systems are important topics for further investigation.

The spin-Peierls transition has been observed in many organic charge transfer compounds, such as TTF-CuBDT.[5, 6, 7, 8, 9, 10] In these systems, a static lattice dimerization has been measured in diffraction experiments. In addition, x-ray measurements of diffuse scattering suggested the presence of a soft phonon associated with the transition[6]. However, direct measurements of the relevant lattice dynamics are lacking due to the unavailability of large crystals for inelastic neutron scattering. The observation of a spin-Peierls transition in the inorganic compound CuGeO<sub>3</sub>[11] rekindled interest

in spin-Peierls research, as large single crystals could be readily grown. However, it is not clear whether CuGeO<sub>3</sub> is a good realization of a conventional spin-Peierls system. The susceptibility does not follow the expected behavior of a spin chain with nearest neighbor coupling[11], and it is believed that significant next nearest neighbor coupling along the chain must be taken into account.[12] In fact, the ratio of the nearest neighbor to next nearest neighbor exchange interaction is close to the critical value for spontaneous formation of a spin gap independent of a lattice distortion.[12] Neutron scattering measurements also reveal a significant magnetic coupling between neighboring chains[13].

Another puzzle in CuGeO<sub>3</sub> is the lack of an observed phonon softening at the transition to the dimerized state. Cross and Fisher developed a theory which includes the spin-phonon coupling and predicts a softening of a spin-Peierls active phonon to zero frequency at  $T_{SP}$ . [4] Neutron studies were unable to detect the presence of this soft phonon, and, in fact, a hardening of phonon modes was observed[14, 15]. Recent theoretical analysis suggests that CuGeO<sub>3</sub> may fall within the “anti-adiabatic” regime (characterized by a large phonon frequency relative to the magnetic interaction energy) where a phonon hardening would be expected[16, 17, 18, 19]. The lattice dynamics associated with the more conventional “adiabatic” regime have yet to be measured in detail.

Recently, a new  $S = 1/2$  spin chain material has been discovered: the transition metal oxide TiOCl. The structure of TiOCl is orthorhombic (Pmmn), consisting of TiO planes (shown in Fig. 1) separated by Cl layers. The Ti<sup>3+</sup> ions are in the  $d^1$  electronic configuration with  $S = 1/2$ . Initially, TiOCl was thought to be an attractive candi-

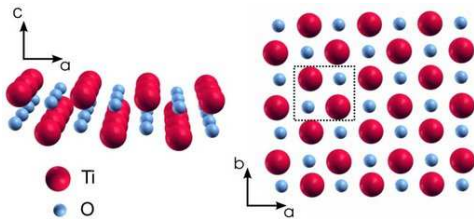


FIG. 1: Structure of TiOCl at high temperatures in the undistorted state. Left: Schematic of a Ti-O layer showing the Ti ion chains along the  $b$ -direction as well as the positions of the oxygens. Right: Schematic of the  $ab$ -plane which more clearly shows the staggered arrangement of adjacent Ti chains. The dashed lines highlight the unit cell.

date for the “resonating valence bond” state[20], but it has since been found to be primarily a one-dimensional magnetic system. Band structure calculations indicate that TiOCl is a Mott insulator with the lowest occupied Ti  $d_{xy}$  orbitals pointed toward each other along the crystallographic  $b$ -direction.[21, 22] The high temperature magnetic susceptibility is well described by the Bonner-Fisher curve, indicating a nearest neighbor magnetic exchange of  $J \simeq 660$  K. [21] In the TiOCl crystal structure, the spin chains are staggered—every other Ti chain is displaced by half a lattice spacing along the  $b$ -direction. Hence, the inter-chain magnetic interaction is frustrated.

Upon cooling, the susceptibility falls away from the Bonner-Fisher curve around  $T \simeq 150$  K and exhibits anomalies at  $T_{c2} = 92$  K and  $T_{c1} = 66$  K.[21] The drop at 150 K has been attributed to the opening of a pseudo-gap [23, 24], the anomaly at 92 K corresponds to the onset of an incommensurately modulated state [23, 25, 26, 27, 28], and the one at 66 K corresponds to a commensurate modulation[29]. Similar behavior has been observed in the isostructural compound TiOBr.[30, 31, 32, 33] At first sight, the observed transitions (such as the incommensurate phase) suggest unconventional spin-Peierls behavior. In order to examine the applicability of a spin-Peierls framework, several issues need to be clarified, such as the nature of the incommensurate phase and the lattice dynamics associated with the structural dimerization.

In this paper, we present x-ray diffraction and inelastic x-ray scattering data on single crystal samples of TiOCl. As we shall show, the material undergoes a spin-Peierls transition in which the structural dimerization occurs in the presence of a soft-phonon at the zone boundary. The low temperature structural modulations are discussed in some detail. The format of the paper is as follows: Section II outlines the crystal growth and thermodynamic characterization of the samples. Section III contains a discussion of the low temperature structures observed with synchrotron x-ray diffraction. Based on measurements of the superlattice peaks, including higher harmonics, we develop a model for the incommensurate structure described by a soliton lattice. In Section IV, the lattice

dynamics are studied using high energy-resolution inelastic x-ray scattering. We observe a soft, zone boundary, phonon mode which drives the spin-Peierls transition, and we compare our data with the Cross-Fisher theory. Finally, Section V contains a discussion and summary of our results.

## II. SAMPLE GROWTH AND CHARACTERIZATION

The single crystals used in this work were grown by the vapor transport method, using the procedure discussed previously[21]. The typical size of an individual crystal was about  $50 \text{ mm} \times 50 \text{ mm} \times 20 \text{ } \mu\text{m}$  along the  $a$ ,  $b$  and  $c$  axes respectively. The magnetic susceptibility was measured on a sample composed of six single crystals co-aligned to within 4 degrees, for a total sample mass of about 8 mg. The susceptibility results (shown in Fig. 2(a) and the inset) were performed using a SQUID magnetometer in an applied magnetic field of 2 Tesla. After the subtraction of a small isotropic Curie tail, the susceptibility curves along the three crystallographic directions

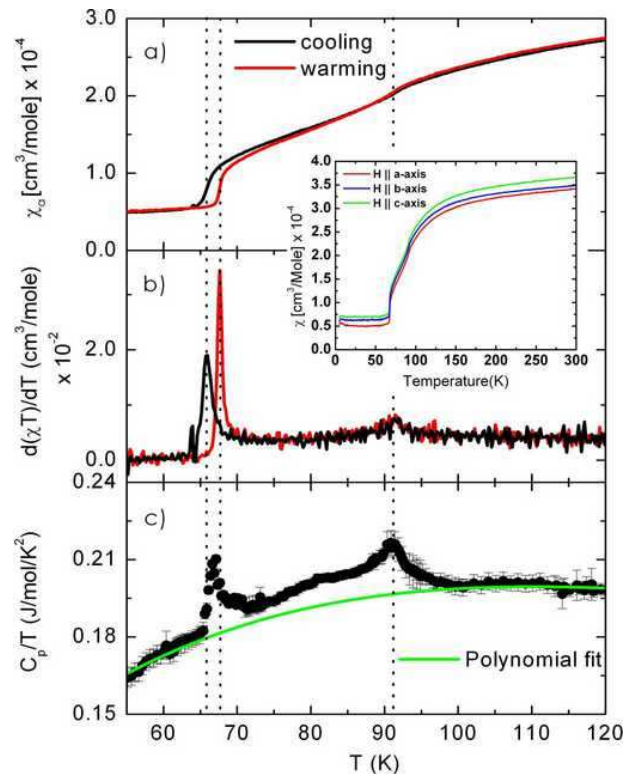


FIG. 2: Thermodynamic characterization of our sample. (a) The magnetic susceptibility upon warming and cooling after the subtraction of a small Curie tail. The sharp drops at  $T_{c2}=92$  K and  $T_{c1} = 66$  K (cooling) indicate the two transition temperatures. Inset: Susceptibility measured along the three crystallographic directions. (b) The quantity  $d(\chi T)/dT$  (c) The specific heat  $C_p(T)$ .

are nearly identical (as shown in the inset), except for a small temperature independent offset, most likely due to anisotropic crystal field contributions. This behavior further indicates the Heisenberg nature of the spins. Moreover, the isotropic drop in the susceptibility is a signature for spin-singlet formation, as opposed to Néel order. Measurements of the susceptibility (Fig.2) upon warming and cooling show hysteretic behavior around  $T_{c1} = 66$  K, which point to a first order phase transition. Hysteresis is not observed around the transition at  $T_{c2} = 92$  K, indicating that this transition is second order in nature. Below  $T_{c1}$ , the susceptibility becomes temperature independent, as seen previously[21], consistent with a fully formed singlet state. This apparent first order transition to the spin-Peierls ground-state seems to differentiate Ti-OCl from the other materials in which a second order spin-Peierls transition is observed([5, 6, 7, 8, 9, 10, 11]). However, as we will show in section VI, we find that it is actually  $T_{c2} = 92$  K which defines the spin-Peierls transition.

Also shown in Fig.2(b) is the quantity  $d(\chi(T)T)/dT$  which should be proportional to the magnetic contribution to the specific heat using the Fisher relation[34, 35]. Indeed, the measured specific heat  $C_p(T)$  in Fig.2(c) shows clear anomalies at  $T_{c1}$  and  $T_{c2}$  which find close correspondence to anomalies in  $d(\chi(T)T)/dT$ . This suggests that the origin of the anomalies in  $C_p(T)$  have a significant magnetic contribution. A rough estimate of the magnetic contribution can be obtained by integrating  $C_p/T$  over  $T$  in order to calculate the change in entropy over the transition region. At these relatively high temperatures, the phonon contribution dominates the specific heat and must be subtracted. We fit the background in the vicinity of the transition region to a fourth order polynomial denoted by the line in the Fig. 2(c). After background subtraction, the integration yields  $\Delta S = 0.04(3)/Nk_B$  for the entropy released in the vicinity of the two transitions. For comparison, one expects  $S/Nk_B \approx (2/3)(k_B T/J)$  for the entropy of a  $S = 1/2$  uniform chain at low-temperatures [34]. Using  $J/k_B = 660$  K[21] and taking  $T$  to be an average of  $T_{c1}$  and  $T_{c2}$  yields a rough upper bound for the change in magnetic entropy of  $\Delta S/Nk_B \simeq 0.08$ . In a previous specific heat study, Hemberger *et al.*[36] estimated a value of 0.12 for  $S/Nk_B$ , obtained by integrating over a wider temperature range. Our estimate is only meant to account for the changes in the near vicinity of  $T_{c1}$  and  $T_{c2}$ , since the subtracted background must also contain a weakly temperature dependent magnetic contribution. Within the errors, our results suggest a significant portion of the entropy change at the transitions is magnetic in origin.

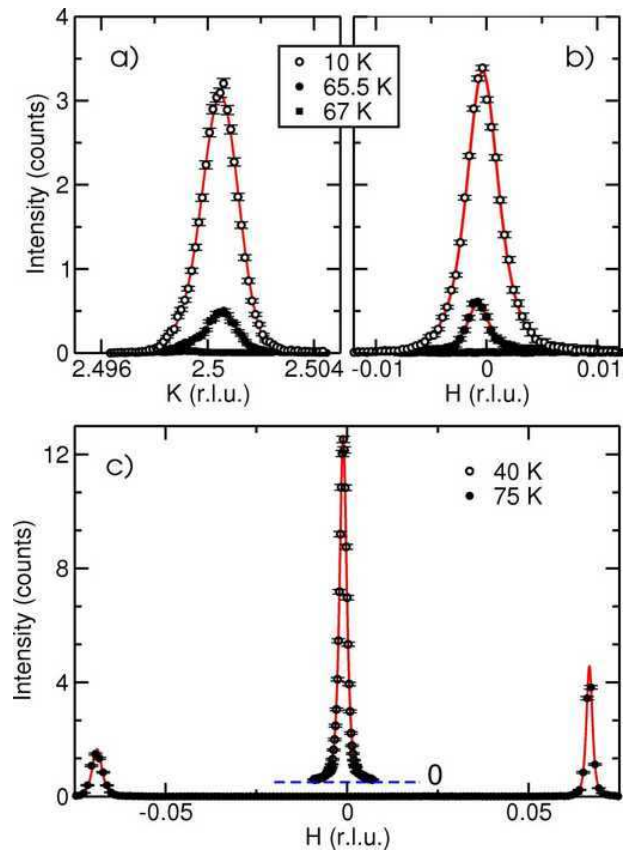


FIG. 3: X-ray diffraction on a single crystal. (a) Longitudinal scans and (b) transverse scans through the (0, 2.5, 0) commensurate position. (c) Scans along  $H$  through the incommensurate and commensurate peak positions. The scans through the incommensurate peaks were performed at a different value of  $K$  than the commensurate peak.

### III. SINGLE CRYSTAL X-RAY DIFFRACTION

#### A. Superlattice Peaks

Synchrotron x-ray scattering measurements were performed on our single crystal samples using the X20A and X22C beamlines at the National Synchrotron Light Source at Brookhaven National Laboratory. The samples were cooled using closed-cycle  $^4\text{He}$  refrigerators. Upon cooling below  $T_{c1} = 66$  K, superlattice peaks were observed at positions displaced from the fundamental Bragg peaks by commensurate wavevectors  $(0, \pm\frac{1}{2}, 0)$ . This indicates doubling of the unit cell along the  $b$ -direction, consistent with a dimerization of the lattice. Scans along  $H$  and  $K$  through the (0, 2.5, 0) superlattice peak (shown in Fig. 3(a) and (b)) are resolution-limited, indicating that the dimerized structure has long-range order. The integrated intensities of 45 fundamental superlattice peaks were measured and used to determine the dimerized structure. The intensities were fit using a model with two adjustable parameters:  $\delta$  (the Ti ion displacement along the  $b$ -direction) and  $\tau$  (the relative shift of neigh-

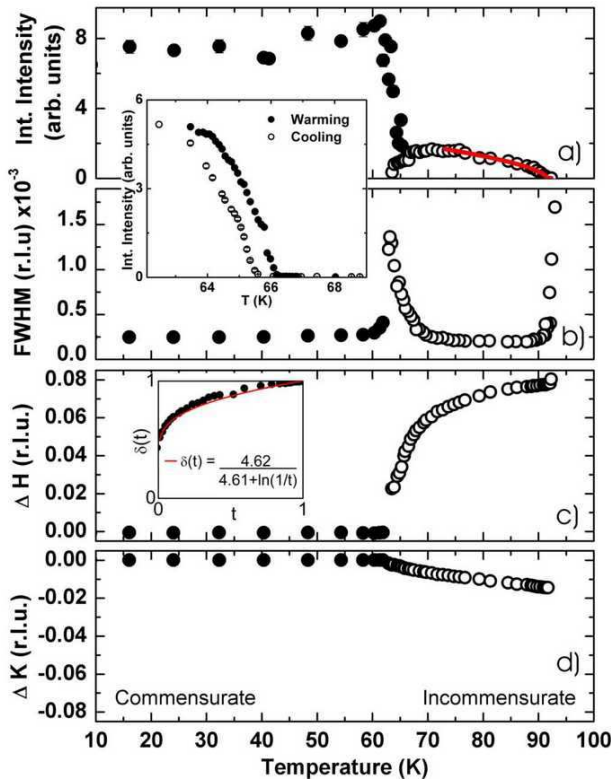


FIG. 4: Temperature dependence of several fitted parameters for the commensurate and incommensurate superlattice peaks. a) The integrated intensity, where the closed symbols refer to a commensurate peak and the open symbols refer to an incommensurate peak. b) The full-width at half-maximum (FWHM) along the  $H$ -direction. Inset: Hysteresis in temperature of the commensurate peak intensity. c) and d) The components  $\Delta H$  and  $\Delta K$  of the displacement wave vector from the commensurate position. Inset: Normalized displacement wave vector for the incommensurate modulation compared with a theoretical prediction involving discommensurations.

boring Ti chains along the  $b$ -direction). Note that once the chains are dimerized, there is no symmetry preventing a relative shift  $\tau$  between the two chain sublattices. The best fit values are  $\delta = 0.03(1)b$ , and  $\tau = 0.05(2)b$ . For simplicity, our model neglected displacements of the Cl and O atoms, yet we still find good agreement with the refinement parameters of Shaz *et al.* for the dimerized state [29].

The temperature dependence of the integrated intensity of the  $(0, 2.5, 0)$  superlattice peak is shown in Fig. 4(a) as the closed circles. Upon warming, the intensity abruptly drops at  $T_{c1} = 66$  K, the same temperature at which our thermodynamic measurements indicate a first order transition. In fact, the intensity of the commensurate superlattice peak also exhibits a thermal hysteresis, shown in the inset, with a width for the hysteresis loop similar to that measured for the susceptibility. Therefore, both magnetic and structural probes indicate the first order nature of transition at  $T_{c1}$ .

Upon warming above  $T_{c1} = 66$  K, the structure has

an incommensurate modulation[23, 25, 26, 27, 28], as shown in Fig. 3(c). That is, between  $T_{c1}$  and  $T_{c2} = 92$  K, superlattice peaks are found at positions displaced from the fundamental positions by wave vectors  $(\pm\Delta H, \frac{1}{2} \pm \Delta K, 0)$ . Here, the incommensurate wave vectors are shifted from the commensurate wave vector  $(0, \frac{1}{2}, 0)$  by the displacement vectors  $(\pm\Delta H, \pm\Delta K, 0)$ . The widths along the  $H$ -direction of both the commensurate and incommensurate peaks are plotted in Fig. 4(b). Both sets of peaks are found to be resolution-limited, indicating long correlation lengths (greater than 2000 Å), except for narrow temperature ranges in the vicinities of  $T_{c1}$  and  $T_{c2}$ . Along the  $K$ -direction, the peaks remain resolution-limited over the measured temperature range. The incommensurate wave vectors continuously change as a function of temperature, and upon cooling approach the commensurate wave vector. The values for  $\Delta H$  and  $\Delta K$  for an incommensurate peak displaced from  $(0, 2.5, 0)$  are plotted as a function of temperature in Figs. 4(c) and (d). The magnitude for  $\Delta H$  is about a factor of 5 larger than  $\Delta K$  at temperature immediately below  $T_{c2} = 92$  K. The temperature dependence of the integrated intensity for the incommensurate peak is shown in Fig. 4(a). The solid line denotes a fit to a power law  $(T - T_{c2})^\beta$  with  $\beta = 0.3$ . Unlike the transition at  $T_{c1}$ , the transition at  $T_{c2}$  appears second order in nature.

## B. Model of the Incommensurate Structure

Since the magnitudes of  $\Delta H$  and  $\Delta K$  for the incommensurate phase are much smaller than  $\frac{1}{2}$  (in reciprocal lattice units), the structure may be thought of as an incommensurate modulation of the dimerized structure. In  $\text{CuGeO}_3$ , the dimerized lattice of the ground state of becomes incommensurate when a large enough magnetic field is applied. The incommensurate structure has been interpreted as a lattice of solitons which proliferate along the chains, separating locally dimerized regions. In  $\text{CuGeO}_3$ , the soliton lattice produces a modulation along the chain direction only, hence the incommensurate wave vector has a non-zero component along the chain direction only. In  $\text{TiOCl}$ , the incommensurate wave vector is displaced from the commensurate position by two components:  $\Delta H$  and  $\Delta K$ , hence, it is slightly more complicated.

As an initial comparison, the temperature dependence of the displacement wave vector magnitude  $\Delta Q = \sqrt{\Delta H^2 + \Delta K^2}$  is plotted in the inset of Fig. 3(c) and compared to a Landau theory prediction. Incommensurate-to-commensurate lock-in transitions have been observed in charge density wave systems, such as  $\text{TaSe}_2$ [37, 38], upon cooling. McMillan[39] used a Landau expansion of the lattice free energy to calculate the temperature dependence of  $\Delta Q$  assuming that the deviations from the commensurate wave vector take the form of long wavelength phase distortions or *discommensurations*. The line in the inset of Fig. 3(c) is the theory



prediction[39],

$$\delta(t) = 4.62/[4.61 + \ln(1/t)], \quad (1)$$

where  $t = (T - T_{c1})/(T_{c2} - T_{c1})$  and  $\delta(t) = \Delta Q(t)/\Delta Q(t=1)$ . This prediction is a universal function of  $t$ , and there are no adjustable parameters in the comparison. The theory roughly captures the singular behavior as  $\delta \rightarrow 0$  near  $T_{c1}$ , suggesting that the incommensurate phase in TiOCl may be described using a model of discommensurations separating commensurate, dimerized regions. Intensity contour plots at different temperatures are shown in Fig. 5(a), showing how the incommensurate peak positions converge to the commensurate position as the temperature is cooled to  $T_{c1}$ . The observed broadening of the peaks just above  $T_{c1}$  makes it difficult to comment on possible phase coexistence[24] or a discontinuous change in wave vector at the incommensurate-to-commensurate transition.

To obtain a more specific picture of the incommensurate modulation, we measured the intensities of several incommensurate superlattice peaks in the vicinity of the  $(0, 1.5, 0)$  position. At  $T = 79$  K, we find four peaks near  $(0, 1.5, 0)$  displaced by wave vectors  $(\pm\Delta H, \pm\Delta K, 0)$  as depicted in the intensity map of Fig. 5(b). All four of these peaks have the same magnitude for the displacement vector, and we call these the first harmonic peaks. We were able to observe third harmonic peaks displaced by  $(\pm 3\Delta H, -3\Delta K, 0)$  from  $(0, 1.5, 0)$ , also shown in Fig. 5(b). This is the first time the higher harmonic peaks have been observed, and their positions and intensities provide crucial insight into the behavior of the incommensurate modulation. No signal above the background could be observed at positions displaced by  $(\pm 3\Delta H, +3\Delta K, 0)$  indicating that the intensities of those peaks are very weak. These observations allow us to rule out a model consisting of the superposition of two independent modulations along the  $a$  and  $b$  directions, as this would not yield third harmonic scattering at the observed positions.

We analyze the intensities using a model which depends on the real-space displacement vectors  $\vec{u}_i$  of the atoms in TiOCl from their equilibrium positions. The resulting structure factor is

$$S(\vec{Q}) = \sum_i f_i(Q) e^{i\vec{Q} \cdot (\vec{R}_i + \vec{u}_i)}. \quad (2)$$

where  $f_i(Q)$  is the form factor for atom  $i$  and the summation is performed over an enlarged supercell for the modulated structure. For simplicity, we only consider displacements of the Ti atoms, leaving the O and Cl atoms at their equilibrium positions, and relegate the displacements to be along the  $b$ -direction.

To construct the observed in pattern in Fig. 5(b), we begin by noting that the continuous evolution of  $\Delta H$  and  $\Delta K$  with temperature indicates that the modulation is truly incommensurate. Hence, we first consider the

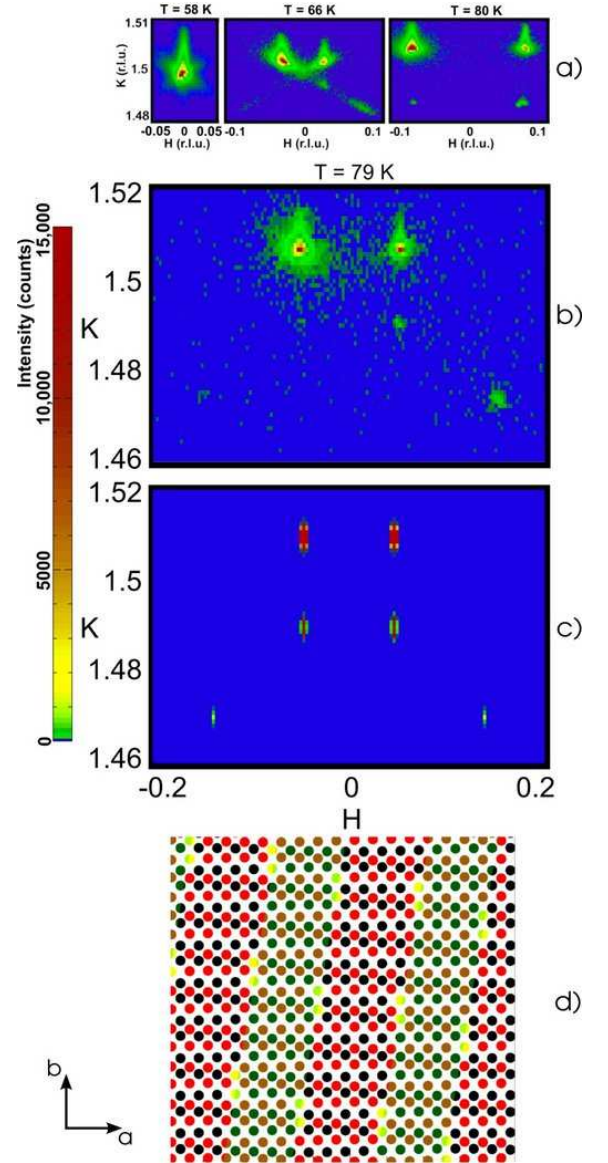


FIG. 5: (a) Series of intensity contour plots showing the temperature evolution of the superlattice peaks (b) Contour plot of the incommensurate peak data at  $T = 79$  K showing both the first and third harmonics. (c) Calculation of the intensity based on our model of the incommensurate structure, as discussed in the text. (d) Real-space picture of the Ti atom positions in the incommensurate structure. Alternate Ti chains have different colors (black and red) for easier viewing. The shaded (unshaded) domains delineate approximate regions with the same relative shift  $+\tau$  ( $-\tau$ ) between adjacent chains. The lightly colored atoms (yellow) on the domain walls denote solitons.

following sinusoidal form for displacements along the  $b$ -direction for a single chain:

$$u(n) = \delta \cos\left(\frac{2\pi n}{\lambda}\right), \quad (3)$$

where the integer  $n$  refers to the  $n$ th Ti atom along  $b$ ,

$\delta$  is the amplitude of the distortion, and  $\lambda$  is the wavelength of the modulation (in units of  $b$ ). The case of  $\lambda = 2$  corresponds to a simple lattice dimerization and is shown in Fig. 6(a) along with a reciprocal space map of the corresponding commensurate superlattice peak. An incommensurately modulated structure can be obtained by making  $\lambda$  slightly larger or smaller than 2. Figure 6(b) shows a modulation with  $\lambda = 2.04$  along with the corresponding superlattice peak pattern.

We observe significantly higher intensities for the first harmonic peaks displaced by  $+\Delta K$  from  $(0, 1.5, 0)$  relative to those displaced by  $-\Delta K$  (Fig. 5(b)). This naturally arises when one considers the two different Ti chains in the unit cell. By varying the relative phase shift  $\phi$  between the modulations on the two chains, different intensity ratios can be obtained. Figure 6(c) shows the diffraction pattern corresponding to a unit cell with Ti chains whose modulations differ by a relative phase shift  $\phi = 0.3\pi$ . The resulting structure factor reproduces the observed intensity asymmetry.

Since the modulation is not simply along the  $b$ -direction (both  $\Delta H$  and  $\Delta K$  are non-zero in the incommensurate phase), we add an additional phase difference,  $\xi$ , between neighboring pairs of Ti chains. The final expression for the displacements is written as

$$u(n, m) = \delta \cos \left( \frac{2\pi n}{\lambda} + j\phi + \xi m \right) \quad (4)$$

where  $j = 0, 1$  labels the two different Ti chains within the unit cell and the integer  $m$  refers to the  $m$ th pair of Ti chains along the  $a$ -direction. A schematic for this modulation is shown in Fig. 6(d). The addition of the phase shift  $\xi m$  has the effect of rotating the modulation direction. The calculated third harmonic peak positions fall on the same line connecting the first harmonic peaks on either side of  $(0, 1.5, 0)$ , as seen in the data. This is *direct* evidence for a one-dimensional (single wave) modulation describing the incommensurate phase of TiOCl. Now, there is a degeneracy between displacements with opposite signs in front of  $\phi$  and  $\xi$ . This gives rise to two twin domains. By considering the other modulated twin domain, the pattern in Fig. 5(c) is obtained. There is good agreement with the calculated intensity ratios in Fig. 5(c) and the observed ones in Fig. 5(b). In addition, all of the peak positions are reproduced. We can also deduce the population factors of the two twin domains to be about 60% and 40%. In order to reproduce the relative intensities of the third harmonics, we used a value for  $\delta$  of  $0.2b$ , which is unrealistically large. This indicates that deviations from a pure sinusoidal modulation exist, as we discuss below in the context of the higher harmonics peaks.

Figure 5(d) shows the real space positions of the Ti atoms in our model for the modulation (in a single twin domain). The adjacent staggered Ti chains are colored differently (red and black) for easier viewing. A local dimerization of the lattice is readily seen throughout the plotted structure, where adjacent Ti chains appear to

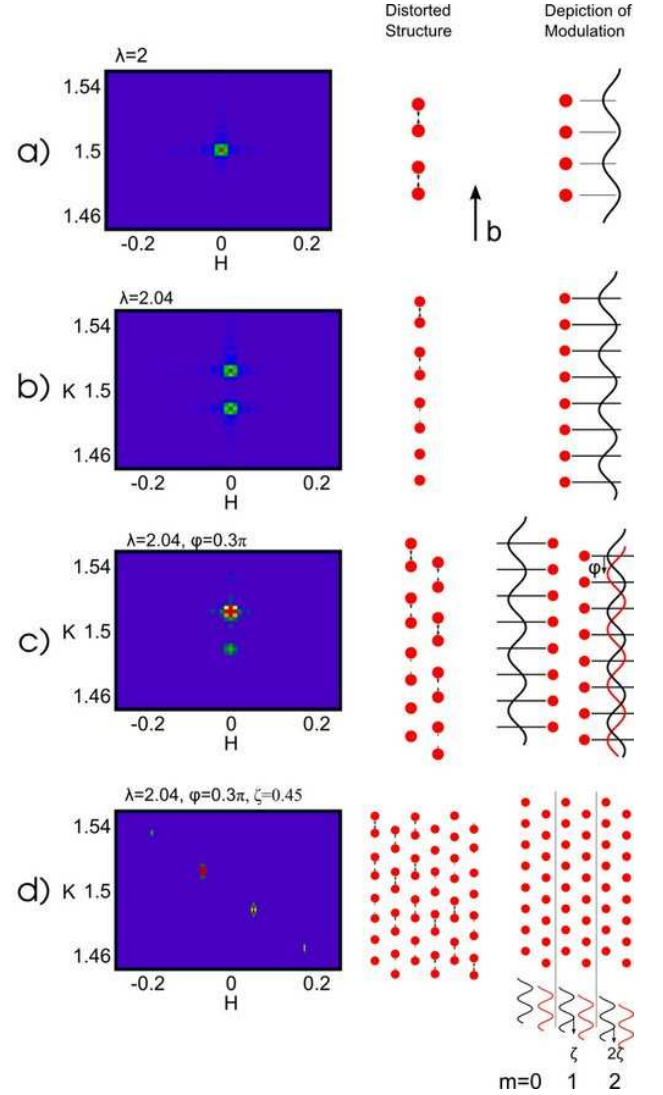


FIG. 6: Real-space depictions of structural modulation along with corresponding reciprocal space maps of the structure factor. (a) Sinusoidal modulation for a single chain which yields a commensurate structure. (b) Incommensurate modulation obtained by changing the wavelength of the sinusoid. (c) Modulation for two adjacent Ti chains, where the value for the relative phase shift  $\phi$  yields an asymmetry in the intensities of the first harmonic peaks. (d) Model for the incommensurate modulation in TiOCl, obtained by phase shifting the modulation of each unit cell along the  $a$ -direction.

have a small relative shift  $\tau$  along the chain direction. For convenience of viewing, each shaded (unshaded) region approximately delineates a single phase domain consisting of the same relative shift  $+\tau$  ( $-\tau$ ). Note that shift  $\tau$  is not a parameter in the above model, but it naturally arises once  $\phi$  and  $\xi$  are specified. On the boundaries between domains (discommensurations), we find Ti atoms which are nearly undimerized (colored yellow in Fig. 5(d)). These correspond to locations where  $u(n, m) \simeq 0$  and may be referred to as solitons. Due to the sinusoidal form of the modulation in our calculation,

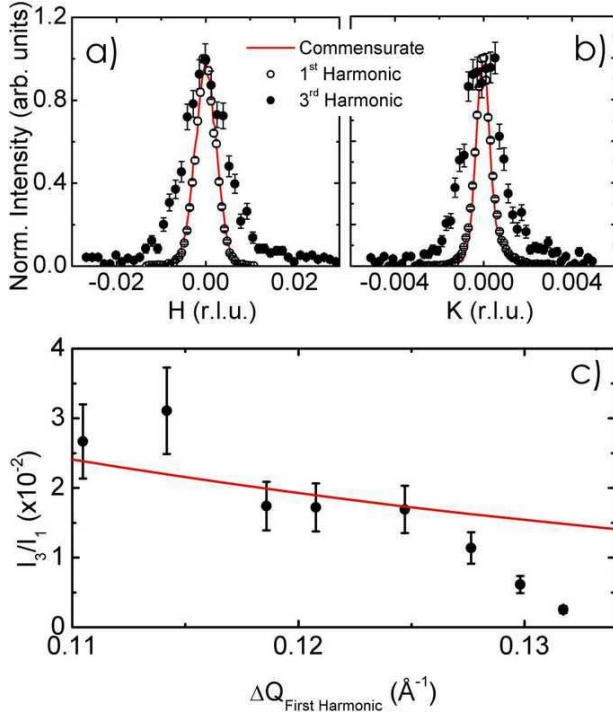


FIG. 7: (a) and (b) Scans through the commensurate, first harmonic incommensurate, and third harmonic incommensurate peaks along the  $H$  and  $K$  directions. The center of each peak was offset in order to plot the three scans on the same axis. (c) Ratio of the harmonic peak intensities  $I_3/I_1$  as a function of the displacement wave vector  $\Delta Q$ . The line is the prediction from the soliton model as described in the text.

the solitons are not well defined, being spread out over many Ti atoms. The other twin domain (with opposite signs of  $\phi$  and  $\xi$ ) is similar to the structure in Fig. 5(d) but with domain walls which tilt in the opposite sense with respect to the vertical chain direction.

Figure 7(a) shows scans along  $H$  and  $K$  through the first and third harmonic peaks at  $T = 79$  K, along with corresponding scans through the commensurate peak at  $T = 10$  K. The center of each peak was offset in order to plot the three scans on the same axis. The first harmonic peak and the commensurate peak are resolution-limited, whereas the third harmonic peak shows a clear broadening. In  $\text{CuGeO}_3$ , Christianson *et al.* [40] observed a slight broadening of the field-induced third harmonic peaks and attribute it to the effects of disorder. They concluded that the incommensurate phase was not long-range ordered in the direction of the broadening, even though it had a long enough correlation length to appear resolution-limited. We believe the same holds true for the incommensurate phase in  $\text{TiOCl}$  in both the  $a$  and  $b$  directions.

The higher harmonic intensities can be calculated by expanding the modulation in terms of the Fourier components; the ratio of harmonic intensities is given by the ratio of the corresponding Fourier coefficients. Here, we

follow an analysis similar to that used to describe the field induced incommensurate modulation in  $\text{CuGeO}_3$  [41, 42]. In  $\text{TiOCl}$ , we note that within a single twin domain, the modulation may be considered to be one-dimensional along the direction given by the displacement wave vector  $(\Delta H, \Delta K, 0)$ . When scattering from a periodic one-dimensional modulation  $u(x)$ , the  $i^{\text{th}}$  harmonic will have intensity [41]

$$I_n \sim \left( \int_0^\pi d\theta \sin(i\theta) \sin[Q u(x)] \right)^2, \quad (5)$$

where  $\theta = qx$  and  $q$  is the reduced wave vector along the modulation direction. For the case of a sinusoidal function, we calculate  $I_3/I_1 \simeq 10^{-8}$  using a displacement amplitude of  $0.03b$ . The measured ratio at  $T = 79$  K is  $I_3/I_1 \simeq 10^{-2}$  and, hence, is not consistent with a pure sinusoidal modulation. In the limit of a square-wave function, we calculate an expected ratio  $I_3/I_1 \simeq 10^{-1}$ , which is larger but closer to the measured ratio.

For a better fit, we consider the Jacobi elliptic function

$$u(l) = \epsilon (-1)^l \text{sn} \left( \frac{\lambda}{\Gamma k}, k \right) \quad (6)$$

where  $l$  denotes a lattice site and the elliptic modulus  $k$  can have values between 0 and 1 ( $k = 0$  corresponds to a sine wave and  $k = 1$  a square wave). The parameter  $\Gamma$  is the soliton half width, and  $\lambda/2$  is equal to the soliton spacing. Then, the ratio  $I_3/I_1$  can be written:

$$\frac{I_3}{I_1} = \left( \frac{Y}{Y^2 + Y + 1} \right)^2. \quad (7)$$

where  $Y = \exp[-\pi K(\sqrt{1-k^2})/K(k)]$ , and  $K$  is the complete elliptic integral of the first kind. The soliton spacing,  $\lambda/2$ , can be written in terms of  $k$  by

$$\frac{\lambda}{2} = \frac{\pi}{\Delta Q} = 2kK(k)\Gamma. \quad (8)$$

At each temperature, the measured values for  $I_3/I_1$  and the magnitude of the displacement wave vector  $\Delta Q$  can be used to determine  $k$  and  $\Gamma$ . For the data in the range  $\Delta Q < 0.125$ , the calculated values for the soliton widths were roughly constant with  $\Gamma = 5(1)$   $\text{\AA}$ , indicating relatively sharp domain walls. By keeping the soliton widths fixed at this value, the expected ratio  $I_3/I_1$  can be calculated as a function of  $\Delta Q$  as shown by the line in Fig. 7(c). The calculated line agrees reasonably well for  $\Delta Q < 0.125$ , lending credence to the soliton lattice description for the incommensurate phase of  $\text{TiOCl}$ . In Fig. 7(c), the data points at larger  $\Delta Q > 0.125$  have  $I_3/I_1$  ratios which are much smaller than the prediction. This means that for these temperatures, which are just below the onset temperature  $T_{c2}$ , the soliton width is considerable larger than  $\Gamma \simeq 5$   $\text{\AA}$  and the modulation is more sinusoidal. For the nearest neighbor Heisenberg model, Nakano and Fukuyama predict [43]  $\Gamma = \frac{\pi Jb}{2\Delta_o}$ , where  $\Delta_o$  is



the magnetic gap. Using  $J = 660$  K[21] and  $\Delta_o = 430$  K [23, 44], this yields  $\Gamma \simeq 8$  Å, which represents an approximate length scale for the soliton width along the chains. The experimental value pertains to the soliton width along the incommensurate modulation, which in TiOCl is not strictly along the chain direction.

Our results lead to the following picture for the sequence of structural changes. Just below  $T_{c2}$ , the structure has a one-dimensional incommensurate modulation of an underlying dimerized state. At first, the envelope function for the modulation has a relatively short wavelength and is approximately sinusoidal. Upon cooling, the wavelength increases and the modulation crosses over from being sinusoidal to being better described by a soliton lattice (with solitons of fixed width). The solitons form domain wall boundaries (or discommensurations) between locally dimerized domains as shown in Fig. 5(d). The domains on either side of the discommensurations may be roughly characterized as having opposite signs for  $\tau$ , the shift parameter between neighboring chains. The soliton spacing (spacing between domain walls) increases with decreasing temperature and diverges at  $T_{c1}$ . At this point, the system wants to become uniformly dimerized, and a single  $\tau$  must be selected. This selection between two degenerate ground states with different symmetries may help explain the first order nature of the transition at  $T_{c1}$ . [45] The above description applies to each twin domain.

Our model, which focuses only on the Ti displacements, is consistent with the structural refinements of Schonleber *et al.*[28]. However, by measuring the higher harmonic content, we have obtained additional details on the structure. The above picture also gives insight into the reason for the incommensurate modulation.[26, 28] Assuming the lattice energy prefers an equal spacing between Ti atoms between chains, then for uniformly dimerized chains, this preference cannot be satisfied due to the staggered nature of the chains. The sinusoidal modulation allows the lattice energy cost to be spread out over many unit cells. As the dimerization amplitude increases, it becomes energetically favorable to form fully dimerized domains at the local level, with the cost in lattice energy being relegated to domain walls. Eventually upon cooling, the magnetic energy gain due to dimerization dominates, and the lattice prefers a uniformly dimerized state with the value for  $\tau$  which minimizes the lattice energy cost.

## IV. INELASTIC X-RAY SCATTERING

### A. Lattice Dynamics

The lattice dimerization which accompanies the spin-Peierls transition is expected to be a displacive structural phase transition. Such displacive transitions are characterized by a softening of a zone-boundary phonon mode which has a polarization similar to that of the

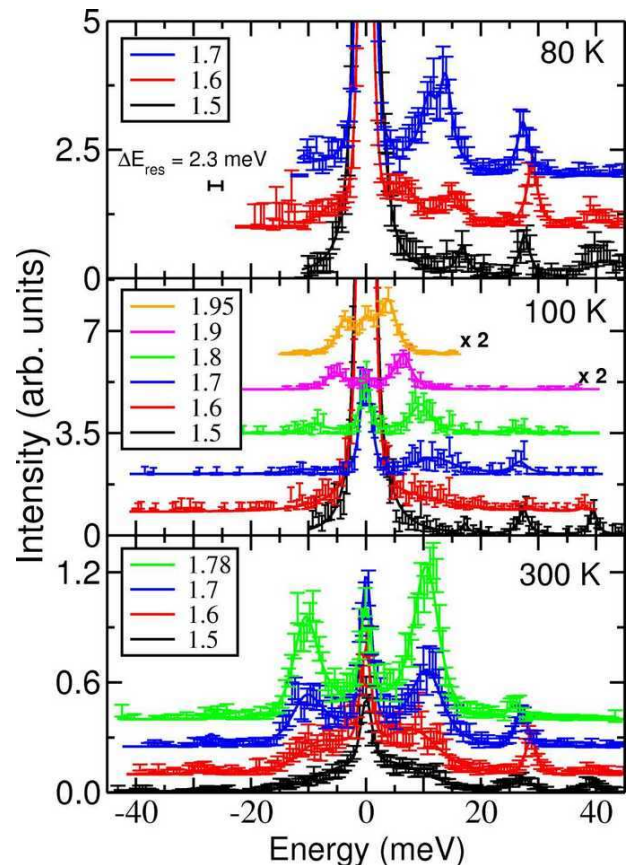


FIG. 8: Energy transfer scans through the phonon excitations at different  $\vec{Q}$  positions along  $(0\ K\ 0)$ , at temperatures of (a)  $T = 80$  K, (b)  $T = 100$  K, and (c)  $T = 300$  K. The solid lines are fits to a damped harmonic oscillator structure factor convoluted with the instrumental resolution as described in the text.

static distortion.[46, 47, 48] This mode softens progressively as the temperature is decreased, until the mode energy reaches zero, and the distortion becomes frozen in. In their theory for the spin-Peierls transition, Cross and Fisher have calculated the expected behavior of such a soft mode.[4] However, to date, the lattice dynamics of a zone-boundary soft phonon in a spin-Peierls system have not been studied. Here, we present a detailed inelastic x-ray scattering characterization of the lattice dynamics in TiOCl. Thus far the only work on the lattice dynamics of TiOCl has been Raman and infrared spectroscopy measurements of the zone center optical modes [45, 49, 50]. The inelastic x-ray scattering technique has the distinct advantage in being able to probe the phonon modes throughout the Brillouin zone. Also, while inelastic neutron scattering requires relatively large crystals, inelastic x-ray scattering can measure very small crystals of interesting new correlated electron systems.

The inelastic x-ray scattering measurements were performed using the SRI-3ID beamline at the Advanced Photon Source at Argonne National Laboratory. An in-line nested channel-cut silicon monochromator and a



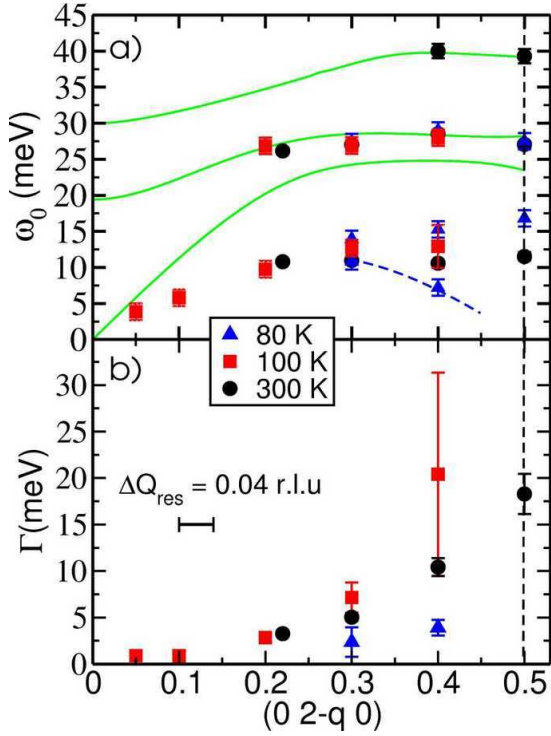


FIG. 9: (a) Dispersion relations for the observed phonon modes where the undamped frequency  $\omega_o$ , extracted from the damped harmonic oscillator fits, is plotted. The lines are predictions from a lattice dynamical calculation. (b) The damping parameter  $\Gamma$  for the lowest energy mode.

bent silicon analyzer in backscattering geometry were used to achieve high energy resolution. By scanning the energy transfer  $\omega$  through the elastic scattering from a plexiglass sample, the energy resolution can be determined. The instrumental resolution function has the following approximate form

$$I(\omega) = I_o \left\{ \frac{2\eta}{\pi\gamma} \left[ 1 + 4 \left( \frac{\omega}{\gamma} \right)^2 \right]^{-1} + (1-\eta) \frac{2}{\gamma} \left( \frac{\ln 2}{\pi} \right)^{1/2} \times \exp \left[ -4 \ln 2 \left( \frac{\omega}{\gamma} \right)^2 \right] \right\}, \quad (9)$$

where  $\gamma$  is the full-width and half-maximum (FWHM),  $I_o$  is the integrated intensity, and  $\eta$  is a mixing parameter [51]. We determined the spectrometer energy resolution to be 2.3 meV FWHM. The data we present below have been corrected for temperature drifts of the monochromator and are normalized by monitor counts.

We performed experiments on two samples of TiOCl, consisting of crystals coigned to within 2-3 degrees with total thicknesses of  $\sim 20 \mu\text{m}$  and  $\sim 40 \mu\text{m}$ . The incident photon energy was 21.3 keV. Representative energy scans are shown in Fig. 8 at temperatures of 80 K, 100 K, and 300 K. For each scan,  $\vec{Q}$  was held constant at various

| Buckingham $Ae^{\frac{L}{r}} - \frac{C}{r^n}$ |         |            |                        | Lattice Parameters |              |            |
|---|---------|------------|------------------------|--------------------|--------------|------------|
| Bond Pair                                     | A (eV)  | $\rho$ (Å) | C (eV Å <sup>3</sup> ) | Lattice par.       | Experimental | Calculated |
| Ti-O  | 2524.38 | 0.29       | 0                      | a(Å)               | 3.786        | 3.784      |
| Ti-Cl   | 2541.81 | 0.29       | 0                      | b(Å)               | 3.361        | 3.368      |
| Cl-Cl   | 8029.88 | 0.33       | 237.7                  | c(Å)               | 8.045        | 8.045      |
| Cl-O  | 8286.91 | 0.26       | 62.2                   |                    |              |            |

| Three Body $\frac{1}{2}k_2(\theta - \theta_0)^2 + \frac{1}{6}k_3(\theta - \theta_0)^3 + \frac{1}{24}k_4(\theta - \theta_0)^4$ |                              |            |                 | Atomic Positions |              |            |
|---|------------------------------|------------|-----------------|------------------|--------------|------------|
| Atoms   | $k_i$ (eV/rad <sup>2</sup> ) | $\theta_0$ | ( $k_1=k_2=0$ ) | Atoms            | Experimental | Calculated |
| Cl-Ti-Cl  | 20.4                         | 90         |                 | Ti (core)        | 0.8807       | 0.8814     |
|   |                              |            |                 | O (core)         | 0.9446       | 0.9586     |
|   |                              |            |                 | Cl (core)        | 0.6680       | 0.6661     |
|   |                              |            |                 | Ti (shell)       | 0.8807       | 0.8794     |
|   |                              |            |                 | O (shell)        | 0.9446       | 0.9600     |
|   |                              |            |                 | Cl (shell)       | 0.6680       | 0.7041     |

TABLE I: Interaction parameters used in the shell model calculation, and the resulting equilibrium crystal parameters.

points along  $(0, K, 0)$  between  $(0, 1.5, 0)$  and  $(0, 2, 0)$ . The scattered intensity is a direct measure of the dynamic structure factor  $S(\vec{Q}, \omega)$  which is related to the dissipative part of the response function by the fluctuation-dissipation theorem. To model the lattice dynamics, we used the damped harmonic oscillator response function:

$$S(\vec{Q}, \omega) = \frac{A_{\vec{Q}}}{\pi} \frac{2\omega\Gamma}{(\omega_o^2 - \omega^2)^2 + \omega^2\Gamma^2} [n(\omega) + 1], \quad (10)$$

where  $\omega_o$  is the undamped phonon frequency,  $\Gamma$  is the damping constant, and  $A_{\vec{Q}}$  is an amplitude. In the underdamped case ( $\omega_o > \Gamma$ ) two inelastic peaks are present at positive and negative energy transfers. In the overdamped case ( $\omega_o < \Gamma$ ) the scattering has the form of a single peak centered about  $\omega = 0$ . In the extreme overdamped limit ( $\omega_o \ll \Gamma$ ) the dynamic structure factor can be rewritten as

$$S(\vec{Q}, \omega) \approx \frac{k_B T}{\hbar\omega_o^2} \frac{1}{\pi} \frac{\gamma}{\gamma^2 + \omega^2}, \quad (11)$$

where  $\gamma = \omega_o^2/\Gamma$  and the high temperature approximation of  $1 + n(\omega) \simeq k_B T/\hbar\omega$  has been used. The solid lines in Fig. 8 are fits to the damped harmonic oscillator cross section convoluted with the instrumental resolution function. In some scans, up to three phonon modes can be fit.

Figure 9(a) shows the fitted values for  $\omega_o$  for all of the observed phonons as a function of the reduced momentum transfer along the  $(0 K 0)$  direction. Note that in this scattering geometry, the cross section is such that only longitudinally polarized phonons are measured. The lowest energy mode corresponds to the longitudinal acoustic branch. The widths of the phonons in this branch are plotted in Fig. 9(b). At  $T = 300$  K (well above  $T_{c2} = 92$  K), the width of the phonon mode increases as  $\vec{Q}$  approaches the zone-boundary. In fact, at the zone-boundary, the fit yields  $\Gamma > \omega_o$  which indicates that the phonon is overdamped. The data at  $T = 100$  K (near  $T_{c2}$ ) show even more dramatic behavior. The width of the phonon mode diverges well before the zone-boundary is reached, indicating that the mode is strongly overdamped. These results are the first indication that the

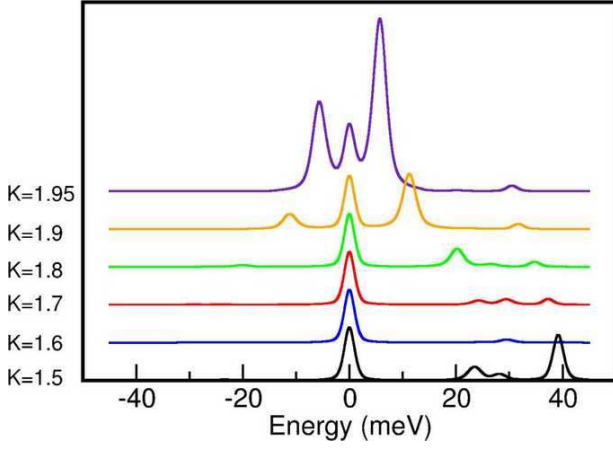


FIG. 10: Calculated cross sections for the longitudinal phonons in the undimerized state at various  $(0\ K\ 0)$  positions, using the eigenvectors and eigenvalues from the lattice dynamical calculation.

longitudinal acoustic phonon at the zone-boundary is a soft mode.

The solid lines in Fig. 9(a) correspond to lattice dynamical calculations for the longitudinal phonon modes based on a shell model using the General Utility Lattice Program [52]. The calculation uses phenomenological potentials to model the strong short-range interactions of the neighboring ions[53]. Four Buckingham potential interactions serve as a repulsive force between atoms, and an additional three-body interaction was used to constrain an angle of  $90^\circ$  for the Ti–Cl–Ti bonding. With these potentials, the system settled into an equilibrium structure nearly identical to the experimental unit cell [54] (see Table I). A comparison between the cal-

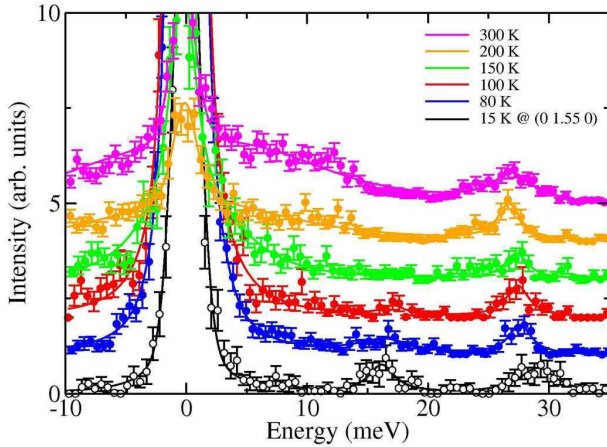


FIG. 11: Energy transfer scans at  $(0, 1.5, 0)$  for different temperatures. The data have been offset for clarity. The  $T = 15$  K data were measured at  $(0, 1.55, 0)$  to avoid contamination from the elastic superlattice peak at  $\omega = 0$ .

culated and observed optic phonons in Fig. 9(a) shows excellent agreement. However, the calculation significantly overestimates the energy for the acoustic branch near the zone boundary, another indication of the soft mode. We note that our calculation and others[55] indicate that this mode is degenerate at the zone boundary. The energy eigenvalues and eigenvectors resulting from the lattice dynamical calculations allow us to calculate the expected scattering intensities using the dynamical structure factor convoluted with the instrumental resolution. This calculation is shown in Fig. 10. The agreement with the observed intensities that we measure is quite good. Again, deviations from the data are apparent for low energies near the zone-boundary due to the presence of the soft mode.

The temperature dependent behavior of the zone boundary phonon is shown in Fig. 11. The data for  $T = 300$  K and  $T = 200$  K were fit to Eq. 10 (the general cross section for the damped harmonic oscillator). However at  $T = 150$  K and below, the fit no longer converged, and Eq. 11 was used for the strongly overdamped case. In this case, it is no longer possible to determine the values of  $\omega_o$  and  $\Gamma$  independently. Useful information can be extracted by noting that the integrated intensity  $I$  is directly proportional to  $T/\omega_o^2$ . Therefore, a plot of

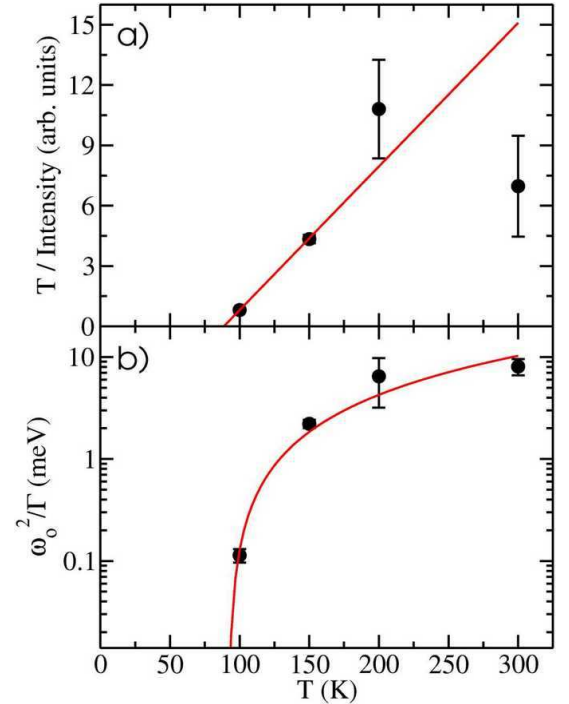


FIG. 12: Behavior of the soft phonon at the zone boundary position  $(0, 1.5, 0)$ . (a) The quantity  $T/\text{Intensity}$  as a function of temperature. The solid line follows the form  $a(T - T_c)$  with  $T_c = 88$  K. (b) The quantity  $\omega_o^2/\Gamma$  as a function of temperature. The solid line serves as a guide to the eye.

$T/I$  versus  $T$  (shown in Fig. 12(a)) should have the same temperature dependence as  $\omega_o^2$ . The solid line has the form  $\omega_o^2 = a(T - T_o)$  which is the result from mean-field theory for a soft-phonon transition,[47, 48] where  $T_o$  is the structural transition temperature and  $a$  is a constant. The fitted line yields  $T_o = 88(2)$  K which closely matches the temperature  $T_{c2} = 92$  K for the onset of the incommensurate superlattice peaks. The quantity  $\omega_o^2/\Gamma$  can also be extracted and is plotted in Fig. 12(b). We see that this quantity plunges to zero around 90 K. This is consistent with  $\omega_o \rightarrow 0$  (accompanied by an increase in  $\Gamma$ ) as expected for a soft phonon transition. Therefore, our inelastic x-ray scattering data provide clear evidence for a soft phonon transition occurring in TiOCl. Specifically, we find that a softening of the longitudinal acoustic phonon at the zone-boundary drives the structural transition to the incommensurate (nearly dimerized) state at  $T_{c2} = 92$  K.

### B. Comparison with the Cross-Fisher Theory

The preceding analysis relied on fits to a phenomenological damped harmonic oscillator model. While this provides strong evidence for the presence of a soft mode, details regarding the microscopic interactions, such as the spin-phonon coupling, cannot be obtained. A general response function which includes such interactions has the form

$$A(\omega) = \frac{1}{\pi} \text{Im} \left[ \frac{1}{\omega^2 - \Omega_0^2 - \Pi(\vec{Q}, \omega)} \right], \quad (12)$$

where  $\Omega_0$  is the harmonic or bare phonon frequency, and  $\Pi(\vec{Q}, \omega)$  is the polarizability (or phonon-self energy). The dynamic structure factor is then given by

$$S(\vec{Q}, \omega) = |S(\vec{Q})|^2 [1 + n(\omega)] A(\omega). \quad (13)$$

By comparing this cross section with that for the damped harmonic oscillator, one can see that  $\Pi(\vec{Q}, \omega)$  contains information regarding the damping. Since  $\Pi(\vec{Q}, \omega)$  is the only term which is complex, it can be broken into real and imaginary parts

$$A(\omega) = \frac{1}{\pi} \frac{\text{Im} [\Pi(\vec{Q}, \omega)]}{(\omega^2 - \Omega_0^2 - \text{Re} [\Pi(\vec{Q}, \omega)])^2 + \text{Im} [\Pi(\vec{Q}, \omega)]^2}. \quad (14)$$

If we then make the substitutions

$$\text{Re} [\Pi(\vec{Q}, \omega)] = \omega_o^2(\vec{Q}, \omega) - \Omega_0^2(\vec{Q}) \quad (15)$$

$$\text{Im} [\Pi(\vec{Q}, \omega)] = \omega\Gamma(\vec{Q}, \omega), \quad (16)$$

we recover the damped harmonic oscillator response function, where  $\omega_0 = \sqrt{\Omega_0^2 + \text{Re}[\Pi]}$ . Here,  $\omega_0$  represents the “quasi-harmonic” frequency which differs from the bare

phonon frequency due to the presence of spin-phonon coupling or other anharmonic interactions.

Cross and Fisher (CF) calculated the polarizability  $\Pi(\vec{Q}, \omega)$  which takes into account the spin-phonon coupling. The phonon system was treated using a mean-field random phase approximation (RPA), whereas the spin dynamics were calculated in a non-perturbative fashion, more accurate than the Hartree approach. Their treatment begins by considering a set of non-interacting spin chains, where each chain is governed by the nearest neighbor Heisenberg Hamiltonian:

$$H_s = \sum_l J(l, l+1) \mathbf{S}_l \cdot \mathbf{S}_{l+1}. \quad (17)$$

Here, the planes of atoms perpendicular to the chains are constrained to move together. Assuming a linear dependence of  $J$  on lattice distortions, the exchange coupling may be written

$$J(l, l+1) = J + \frac{1}{\sqrt{N}} \sum_q g(q) Q(q) e^{iqb} (1 - e^{iqlb}), \quad (18)$$

where  $q$  is the reduced wave vector along the chain direction,  $g(q)$  is the spin-phonon coupling, and  $Q(q)$  denotes the phonon normal mode coordinates. The spin-phonon interaction leads to an expression for the polarizability that depends on the dimer-dimer correlation function  $\langle[(\mathbf{S}_l \cdot \mathbf{S}_{l+1})_t, (\mathbf{S}_0 \cdot \mathbf{S}_1)_{t=0}] \rangle$  which CF calculate using bosonization. It is also possible to calculate the dimer-dimer correlation function using conformal field theory [56], which yields an identical result in the long wavelength limit. The CF polarizability is calculated to be [4]

$$\Pi_{CF}(q, \omega) = -0.37 |(1 - e^{iqb})g(q)|^2 \times I_1 \left( \frac{\omega + c(q - 2k_f)}{2\pi T} \right) I_1 \left( \frac{\omega - c(q - 2k_f)}{2\pi T} \right) \frac{1}{T}, \quad (19)$$

where

$$I_1(k) = \frac{1}{\sqrt{8\pi}} \frac{\Gamma(\frac{1}{4} + \frac{1}{2}ik)}{\Gamma(\frac{3}{4} + \frac{1}{2}ik)}, \quad (20)$$

where  $2k_f = \pi/b$  and  $c = \pi Jb/2$  [57] is the spin-wave velocity. In this treatment, the condition that defines the spin-Peierls phase transition temperature,  $T_{SP}$ , is

$$\omega_o^2 = \Omega_0^2 + \Pi_{CF}(q = 2k_f, \omega \rightarrow 0, T = T_{SP}) = 0. \quad (21)$$

This can be solved to get an expression for the spin-phonon coupling for the zone boundary mode:

$$g = \Omega_0 \sqrt{\frac{\pi}{3.2} T_{SP}}. \quad (22)$$

We now compare our data with the results of Cross and Fisher by fitting our data with the dynamic structure factor that explicitly includes the CF polarizability  $\Pi_{CF}(q, \omega)$  (Eq. 19) convoluted with the instrumental



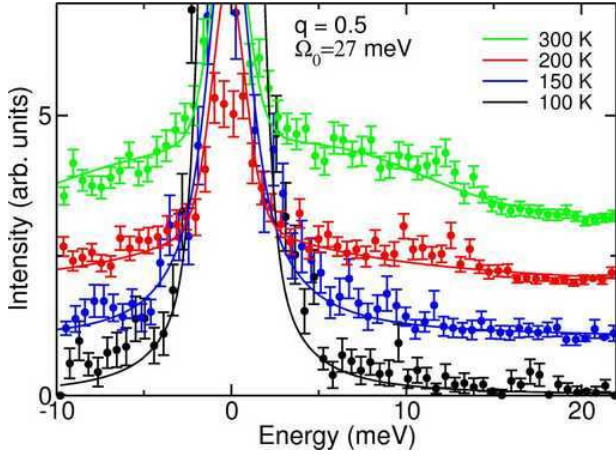


FIG. 13: Energy transfer scans of the low energy phonon mode at the zone boundary. The lines denote fits to the dynamical structure factor calculated using the Cross-Fisher theory.

resolution. Only data in the energy range  $-20 \text{ meV} \leq \omega \leq 20 \text{ meV}$  was fit, thereby focusing on the longitudinal acoustic mode. We first fit data taken the zone boundary position  $(0, 1.5, 0)$  at several temperatures, as shown in Fig. 13. At the zone boundary, the CF polarizability reduces to

$$\Pi_{CF}(q, \omega) = -0.74g^2 \left[ I_1 \left( \frac{\omega}{2\pi T} \right) \right]^2 \frac{1}{T}. \quad (23)$$

Therefore, the only adjustable parameters in the dynamical structure factor are the spin-phonon coupling  $g$  and the bare phonon frequency  $\Omega_0$ . Since  $g^2$  scales with the CF polarizability, a non-zero  $g$  will affect both the peak width and the shift of  $\omega_0$  from  $\Omega_0$ . Away from the zone boundary, the polarizability also depends on  $J$ , therefore  $J$  and  $g$  cannot be fit independently in general.

The solid lines in Fig. 13 represent fits to the dynamical structure factor at  $q = 0.5$  based on the CF theory. Here, we let  $g$  vary with temperature, but kept  $\Omega_0$  fixed at the best fit value of  $\Omega_0 = 27(1) \text{ meV}$ . Letting  $g$  float with temperature was necessary in order to get reasonable fits, and we will comment on this later. Once  $g$  was determined for a given temperature, the scans at other  $q$  positions were then fit with  $\Omega_0$  and  $J$  as the adjustable parameters. For the data sets at  $T = 100 \text{ K}$  and  $T = 300 \text{ K}$ , the analysis yielded a roughly consistent magnetic exchange of  $J \sim 200 \text{ K}$ . This value for  $J$  is about three times smaller than that deduced from the magnetic susceptibility results[21]. However, our value for  $J$  is remarkably close considering that it resulted from measurements of only the *phonon* positions and lineshapes.

The resulting values for the bare phonon frequency  $\Omega_0$  are plotted in Fig. 14(a) as a function of the reduced wave vector  $(0, q, 0)$ . The solid line denotes the prediction from the lattice dynamical calculation discussed in the previous section. Clearly, the bare phonon frequency  $\Omega_0(q)$  follows the calculated dispersion curve much better than

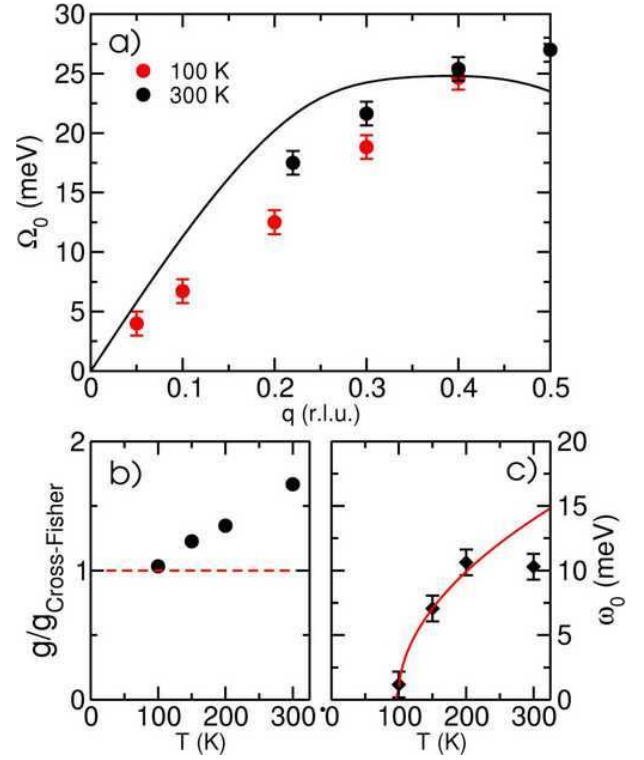


FIG. 14: (a) The bare phonon frequency  $\Omega_0$  of the longitudinal acoustic mode extracted from the fits to the Cross-Fisher theory. The solid line denotes the shell model calculation. (b) The fitted spin-phonon coupling  $g$ , normalized to the value of  $g$  calculated using Eq. 22. (c) The quasi-harmonic frequency  $\omega_0$  of the zone boundary mode, extracted from fits to the Cross-Fisher theory. The solid line denotes the power-law form  $A\sqrt{T - T_c}$  with  $T_c = 98 \text{ K}$ .

the mode energies  $\omega_0$  from the damped harmonic oscillator fits (Fig. 12(a)). Thus, it appears that the CF theory captures the anharmonic effects of the spin-phonon coupling in  $\text{TiOCl}$  reasonably well. However, in order to obtain good fits at all temperatures,  $g$  was allowed to vary. These values are plotted in Fig. 14(b), normalized by the value of  $g$  calculated using Eq. 22 (with  $\Omega_0 = 27 \text{ meV}$  and  $T_{c2} = 92 \text{ K}$ ), which yields  $g_{\text{Cross-Fisher}} = 75 \text{ meV}^{3/2}$ . The figure shows that the fitted values of  $g$  approach  $g_{\text{Cross-Fisher}}$  as  $T \rightarrow T_{c2}$ . Since the fits to the dynamical structure factor were performed without knowledge of  $T_{c2}$ , this result supports the self-consistency and validity of the CF expressions describing the soft phonon near  $T_{SP}$ . We also have enough information to determine the quasi-harmonic frequency  $\omega_0$  at  $q = 0.5$ , which is plotted in Fig. 14(c). We see that the spin-phonon coupling reduces  $\omega_0$  from the bare value  $\Omega_0$  by about a factor of 2. Also, at the spin-Peierls transition,  $\omega_0$  should fall to zero. Indeed, the solid line through the data is a fit to the form  $A\sqrt{T - T_c}$  where  $T_c = 98 \text{ K}$ , which is close to  $T_{c2} = 92 \text{ K}$ . Hence, we identify  $T_{c2}$  as the spin-Peierls transition temperature in  $\text{TiOCl}$ . The congruence with the basic features of the CF theory allows us to conclude

that that TiOCl is, in fact, a good realization of a spin-Peierls system.

While the CF theory can successfully describe many aspects of the phonon data, there are some discrepancies. Such discrepancies are not completely unexpected, since the theory is based on a mean-field RPA treatment of the phonons in which fluctuation corrections due to the phonon dynamics are absent. As noted above, the best fit  $g$  is temperature dependent and the fitted value of  $J$  is a factor of 3 lower than that estimated from the magnetic susceptibility. This likely stems from limits to the applicable range for  $\Pi_{CF}(q, \omega)$ , which is most accurate in the vicinity of  $q \approx 0.5$  and for temperatures near  $T_{SP}$ . In order to more fully describe the data, additional anharmonic effects which broaden the phonon lineshapes away from  $q = 0.5$  must be included. In addition, we observe the zone boundary phonon remains strongly overdamped even at temperatures as high as  $T = 300$  K ( $\gg T_{SP}$ ). These unusual features of the phonon dynamics of TiOCl require better theoretical understanding.

## V. DISCUSSION AND SUMMARY

The TiOCl compound has many ingredients which make it a particularly ideal spin-Peierls system. First, it is composed of weakly interacting  $S = 1/2$  spin chains which are well described by a dominant nearest-neighbor interaction along the chain.[21] The weak magnetic coupling between chains is facilitated by the staggered arrangement of adjacent Ti chains. Indeed, a lattice dimerization is observed at low temperatures, concomitant with spin-gap behavior observed in the susceptibility. However, as a consequence of the staggered Ti chains, an incommensurately modulated phase develops prior to the commensurate dimerization upon cooling. Our detailed x-ray scattering studies have led to considerable new insight into this incommensurate phase. We have developed a model which describes how the Ti chains are modulated relative to each other and shows good agreement with the data. Our analysis of the higher harmonic scattering indicates a cross-over from sinusoidal to a soliton-like modulation as the temperature is reduced below  $T_{c2} = 92$  K. The incommensurate-to-commensurate transition at  $T_{c1} = 66$  K is characterized by a divergence of the domain wall spacing and selection of a single dimerized domain.

TiOCl is also of interest since it is an inorganic material for which single crystal samples can be grown. Using single crystal samples, we have performed high-resolution inelastic x-ray scattering measurements of the lattice dynamics. This is a noteworthy example in which x-rays rather than neutrons can provide the best information on the detailed lattice dynamics of a correlated electron system. We have discovered a soft phonon mode which drives the spin-Peierls transition. This stands in marked contrast to the much studied CuGeO<sub>3</sub> system, for which

a soft phonon has not been observed. In TiOCl, the lattice dynamics suggest that the spin-Peierls temperature is associated with the transition temperature  $T_{c2} = 92$  K, and not  $T_{c1} = 66$  K as has been previously speculated.

Our measurements on TiOCl allow to make an unprecedentedly detailed comparison with the Cross-Fisher theory. We find that the calculated polarizability can successfully describe the measured phonon cross sections. That is, the extracted values for the bare phonon frequencies and spin-phonon coupling give a consistent picture of both the phonon dispersion and the phonon softening at  $T_{SP}$ . However, several discrepancies exist, such as the small value of  $J$  and a temperature dependent spin-phonon coupling constant. This points to the necessity of adding additional anharmonic effects to fully describe the lattice dynamics. Interestingly, the soft phonon mode remains strongly overdamped at temperatures much higher than the observed spin-Peierls transition temperature.

The presence of the soft mode transition indicates that TiOCl falls within the adiabatic regime (i.e., small  $\Omega_0$ ). Indeed, the fitted bare phonon frequency of the Peierls-active mode,  $\Omega_0 \simeq 27$  meV, is smaller than the magnetic energy scale  $J \simeq 57$  meV in the system. Recent theories have expanded upon the Cross-Fisher result and shed further light on the conditions separating the adiabatic and anti-adiabatic regimes.[16, 17, 18, 19] Gros and Werner have shown that within RPA a soft phonon occurs only if  $\Omega_0/T_{SP} < 2.2$ . [16] For TiOCl, we calculate  $\Omega_0/T_c \simeq 2.9$  (using  $T_{c2} = 92$  K as the critical temperature). Hence, their prediction suggests that TiOCl falls outside of the adiabatic regime. However, a more recent theory by Dobry *et al.*[58] goes beyond RPA and takes into account the dynamics of the transverse phonons arising from inter-chain interactions. They find that soft phonon behavior may occur for values as high as  $\Omega_0/T_c \simeq 3$ , provided that  $\omega_{\perp}/T_{SP}$  for the transverse phonon is not very large[58]. Our shell model calculations indicate that the latter condition is satisfied in TiOCl. Of course, further experimental studies of the transverse phonon dynamics would certainly be useful. Also, more theoretical work based explicitly on the structure of staggered Ti chains would be necessary for additional detailed comparisons. With its wealth of observed phenomena and relatively simple crystal structure, TiOCl is an ideal system for quantitative tests of theories for coupled spin and lattice degrees of freedom in one-dimensional magnets.

## Acknowledgments

We thank P. A. Lee, T. Senthil, P. Ghaemi, T. Yildirim, and J. Hill for useful discussions. The work at MIT was supported by the Department of Energy under grant number DE-FG02-04ER46134.

\* email: younglee@mit.edu

- 
- [1] H. Bethe, Z. Phys. **71**, 205 (1931).
- [2] L. Hulthén, Ark. Mat. Astron. Fys. **26A** (1938).
- [3] E. Pytte, Phys. Rev. B **10**, 4637 (1974).
- [4] M. C. Cross and D. S. Fisher, Phys. Rev. B **19**, 402 (1979).
- [5] I. S. Jacobs, J. W. Bray, J. H. R. Hart, L. V. Interrante, J. S. Kasper, G. D. Watkins, D. E. Prober, and J. C. Bonner, Phys. Rev. B **14**, 3036 (1976).
- [6] D. E. Moncton, R. J. Birgeneau, L. V. Interrante, and F. Wudl, Phys. Rev. Lett. **39**, 507 (1977).
- [7] S. Huizinga, J. Kommandeur, G. Sawatsky, B. Thole, K. Kopenga, W. de Jonge, and D. Roos, Phys. Rev. B **19**, 4723 (1979).
- [8] J. W. Bray, J. H. R. Hart, L. V. Interrante, I. S. J. adn J. S. Kasper, G. D. Watkins, S. H. Wei, and J. C. Bonner, Phys. Rev. Lett. **35**, 744 (1975).
- [9] J. P. Pouget, Eur. Phys. J. B **20**, 321 (2001).
- [10] R. J. J. Visser, S. Oostra, C. Vettier, and J. Voiron, Phys. Rev. B **28**, 2074 (1983).
- [11] M. Hase, I. Terasaki, and K. Uchinokura, Phys. Rev. Letters **70**, 3651 (1993).
- [12] J. Riera and A. Dobry, Phys. Rev. B **51**, 16098 (1995).
- [13] L. P. Regnault, M. Ain, B. Hennion, G. Dhalenne, and A. Revcolevschi, Phys. Rev. B **53**, 5579 (1996).
- [14] J. E. Lorenzo, K. Hirota, G. Shirane, J. M. Tranquada, M. Hase, K. Uchinokura, H. Kojima, I. Tanaka, and Y. Shibuya, Phys. Rev. B **50**, 1278 (1994).
- [15] M. Braden, W. Reichardt, B. Hennion, G. Dhalenne, and A. Revcolevschi, Phys. Rev. B **66**, 214417 (2002).
- [16] C. Gros and R. Werner, Phys. Rev. B **58**, 14677 (1998).
- [17] M. Holicki, H. Feshke, and R. Werner, Phys. Rev. B **63**, 174417 (2001).
- [18] E. Orignac and R. Chitra, Phys. Rev. B **70**, 214436 (2004).
- [19] R. Citro, E. Origanac, and T. Giamarchi, Phys. Rev. B **72**, 024434 (2005).
- [20] R. J. Beynon and J. A. Wilson, Journal of Physics: Condensed Matter pp. 1983–2000 (1993).
- [21] A. Seidel, C. A. Marianetti, F. C. Chou, G. Ceder, and P. A. Lee, Phys. Rev. B **67**, 020405 (2003).
- [22] M. Hoinkis, M. Sing, J. Schfer, M. Klemm, S. Horn, H. Benthien, E. Jeckelmann, T. Saha-Dasgupta, L. Pisani, R. Valenti, et al., Phys. Rev. B **72**, 125127 (2005).
- [23] T. Imai and F. C. Chou, cond-mat/0301425 (2003).
- [24] J. P. Clancy, B. D. Gaulin, K. C. Rule, J. P. Castellán, and F. C. Chou, Phys. Rev. B **75**, 100401 (2007).
- [25] E. Abel, K. Matan, F. C. Chou, and Y. S. Lee, Bull. Amer. Phys. Soc. **49**, 317 (2004).
- [26] R. Rückamp, J. Baier, M. Kriener, M. Haverkort, T. Lorenz, G. Uhrig, L. Jongen, A. Möller, G. Meyer, and M. Grüninger, Phys. Rev. Lett. (2005).
- [27] A. Krimmel, J. Strempfer, B. Bohnenbuck, B. Keimer, M. Hoinkis, M. Klemm, S. Horn, A. Loidl, M. Sing, R. Claessen, et al., Phys. Rev. B **73**, 172413 (2006).
- [28] A. Schönleber, S. van Smaalen, and L. Palatinus, Phys. Rev. B **73**, 214410 (2006).
- [29] M. Shaz, S. v. Smaalen, L. Palatinus, M. Hoinkis, M. Klemm, S. Horn, and R. Claessen, Phys. Rev. B **71**, 100405 (2005).
- [30] P. Lemmens, K. Choi, R. Valent, T. Saha-Dasgupta, E. Abel, Y. Lee, and F. Chou, New J. Phys. **7**, 74 (2005).
- [31] S. van Smaalen, L. Palatinus, and A. Schonleber, Phys. Rev. B **72**, 020105 (2005).
- [32] T. Sasaki, M. Mizumaki, T. Nagai, T. Asaka, K. Kato, M. Takata, Y. Matsui, and J. Akimitsu, Physica B **378-80**, 1066 (2006).
- [33] T. Sasaki, M. Mizumaki, T. Nagai, T. Asaka, K. Kato, M. Takata, Y. Matsui, and J. Akimitsu, cond-mat/0509358 (2005).
- [34] D. C. Johnston, R. K. Kremer, M. Troyer, X. Wang, and A. Klumper, Phys. Rev. B **61**, 9558 (2000).
- [35] M. Fisher, Philos. Mag. **7**, 1731 (1962).
- [36] J. Hemberger, M. Hoinkis, M. Klemm, M. Sing, R. Claessen, S. Horn, and A. Loidl, Phys. Rev. B **72**, 012420 (2005).
- [37] D. E. Moncton, J. D. Axe, and F. J. DiSalvo, Phys. Rev. B **16**, 801 (1977).
- [38] R. M. Fleming, D. E. Moncton, D. B. McWhan, and F. J. DiSalvo, Phys. Rev. Lett. **45**, 576 (1980).
- [39] W. McMillan, Phys. Rev. B **14**, 1496 (1976).
- [40] R. J. Christianson, Y. J. Wang, S. C. LaMarra, R. J. Birgeneau, V. Kiryukhin, T. Masuda, I. Tsukada, K. Uchinokura, and B. Keimer, Phys. Rev. B **66**, 174105 (2002).
- [41] V. Kiryukhin, B. Keimer, J. P. Hill, and A. Vigliante, Phys. Rev. Lett. **76**, 4608 (1996).
- [42] V. Kiryukhin, B. Keimer, J. P. Hill, S. M. Coad, and D. M. Paul, Phys. Rev. B **54**, 7269 (1996).
- [43] T. Nakano and H. Fukuyama, J. Phys. Soc. Jpn. **50**, 1679 (1980).
- [44] P. J. Baker, S. J. Blundell, F. L. Pratt, T. Lancaster, M. L. Brooks, W. Hayes, M. Isobe, Y. Ueda, M. Hoinkis, M. Sing, et al., Phys. Rev. B **75**, 094404 (2007).
- [45] D. Fausti, T. Lummen, C. Angelescu, R. Macovez, J. Luzon, R. Broer, P. Rudolf, P. van Loosdrecht, N. Tristan, B. Buchner, et al., cond-mat/0704.017 (2007).
- [46] G. Shirane, J. D. Axe, and J. Harada, Phys. Rev. B **2**, 3651 (1970).
- [47] S. M. Shapiro, J. D. Axe, and G. Shirane, Phys. Rev. B **6**, 4332 (1972).
- [48] G. Shirane, Reviews of Modern Physics **46**, 437 (1974).
- [49] P. Lemmens, K. Y. Choi, G. Caimi, L. Degiorgi, N. N. Kovaleva, A. Seidel, and F. C. Chou, Phys. Rev. B p. 134429 (2004).
- [50] G. Caimi, L. Degiorgi, N. Kovaleva, P. Lemmens, and F. Chou, Phys. Rev. B **69**, 125108 (2004).
- [51] H. Sinn, E. E. Alp, A. Alatas, J. Barraza, G. Bortel, E. Burkel, D. Shu, W. Sturhahn, J. Sutter, T. Toellner, et al., Nuclear Instruments and Methods in Physics Research A **467-468** (2), 1545 (2001).
- [52] J. D. Gale and A. L. Rohl, Mol. Simul. **29**, 291 (2003).
- [53] J. Gale and A. Rhol, *General utility lattice program*, <http://www.ivec.org/GULP/>.
- [54] H. Schäfer, F. Wartenpfer, and E. Weise, Z. Anorg. Allg. Chem. **295**, 268 (1958).
- [55] T. Yildirim, *private communication*.
- [56] P. Ghaemi, *private communication*.
- [57] J. des Cloiseaux and J. Pearson, Phys. Rev. **128**, 2131 (1962).
- [58] A. Dobry, D. C. Cabra, and G. L. Rossini, Phys. Rev. B **75**, 045122 (2007).